On the nature of radial transport across sheared zonal flows in electrostatic ion-temperature-gradient gyrokinetic tokamak plasma turbulence

R. Sánchez,[1] D. E. Newman,[2] J.-N. Leboeuf,[3] B. A. Carreras,[4] and V. K. Decyk[5]
[1]*Fusion Energy Division, Oak Ridge National Laboratory, Oak Ridge, Tennessee 37831-8071, USA*
[2]*Department of Physics, University of Alaska, Fairbanks, Alaska 99775-5920, USA*
[3]*JNL Scientific, Inc., Casa Grande, Arizona 85294-9695, USA*
[4]*BACV Solutions, Inc., Oak Ridge, Tennessee 37830-8222, USA*
[5]*UCLA, Los Angeles, California 90095-1547, USA*

It is argued that the usual understanding of the suppression of radial turbulent transport across a sheared zonal flow based on a reduction in effective transport coefficients is, by itself, incomplete. By means of toroidal gyrokinetic simulations of electrostatic, ion-temperature-gradient turbulence, it is found instead that the character of the radial transport is altered fundamentally by the presence of a sheared zonal flow, changing from diffusive to anticorrelated and subdiffusive. Furthermore, if the flows are self-consistently driven by the turbulence via the Reynolds stresses (in contrast to being induced externally), radial transport becomes non-Gaussian as well. These results warrant a reevaluation of the traditional description of radial transport across sheared flows in tokamaks via effective transport coefficients, suggesting that such description is oversimplified and poorly captures the underlying dynamics, which may in turn compromise its predictive capabilities.

I. INTRODUCTION

During the last few decades, the beneficial role played by a sheared zonal flow for tokamak plasma confinement has been increasingly recognized, both experimentally, with the advent of the *H*-mode in the 80's (Ref. 1) and other enhanced confinement regimes exhibiting internal transport barriers,[2,3] theoretically,[4–6] and numerically.[7,8] These sheared flows are central for the advanced regimes in which the future ITER tokamak will operate.[9] The benefits for confinement coming from the presence of sheared poloidal flows are by no means restricted to tokamaks but are also well documented in other plasma confinement devices such as stellarators[10] and reverse-field pinches.[11]

The traditional understanding of how the suppression of radial transport by a sheared zonal flow takes place can be sketched as follows: the turbulent radial flux of any quantity s can be expressed as $\tilde{\Gamma}_r=\langle\tilde{s}\tilde{v}_r\rangle$, where $\tilde{s}$ represents the fluctuating advected field and $\tilde{v}_r$ is the fluctuating radial velocity. This flux can be decreased due to either a reduction in the amplitude of any of the fluctuating fields[4] or to an appropriate shift in the phase between advected and advecting fields.[12] The details of how this suppression happens are however often complicated and still not well understood in many cases. Mostly for that reason, the investigation of these various possibilities in a tokamak geometry is traditionally done by assuming *ab initio* that some effective diffusivity can be used to characterize radial transport in the absence of any poloidal (and toroidal) flow. Say, $D_r\sim V_c^2/l_r$, where l_r is the mean (radial) eddy size and V_c is a typical value for the fluctuating radial velocity, from which a characteristic time scale for the process $\tau\sim l_r/V_c$ follows. (The argument that follows will also hold for other choices since it only requires that typical scales can be defined.) Then, it is assumed that the radial flux is reduced because of the changes in l_r and V_c (and thus τ) brought about by the action of the radially sheared poloidal flow on the turbulence. The key point here is to note that for this argument to be valid, an additional hypothesis (usually assumed implicitly) must be accepted: that the nature of radial transport must be and remain diffusive. Or more precisely, that the underlying transport dynamics must be and remain Gaussian and Markovian, so that finite values for V_c, l_r, and τ still exist. In this invited paper, we review and extend the recent work[13] aimed at testing the validity of such a hypothesis. As we will show, the answer is negative in the simulations investigated, which suggests the need for revisiting our understanding of transport suppression by sheared flows. The second aspect is the quantification of the dynamical differences that exist between the suppression of radial transport carried out by a radially sheared poloidal flow that is driven externally with respect to the case in which the flow is driven by the turbulence itself via the turbulent Reynold stresses.[6] In both fluid and gyrokinetic simulations, it has been observed for years that these two situations can behave quite differently from a dynamical point of view.[7,14,15] However, the suppression of radial transport in both cases is still encapsulated within the same effective diffusivity scheme mentioned earlier, especially in the context of modeling transport over the much longer tokamak confinement time scales. From this investigation, we expect that better effective transport models can be found to deal with these cases.

Our studies have been done with toroidal gyrokinetic simulations of global, electrostatic ion-temperature-gradient

(ITG) turbulence carried out with the UCAN gyrokinetic code.[16] In Sec. I, after reviewing the fundamentals of UCAN, we describe the simulations that have been used for these studies. In Sec. II, we briefly review the theoretical aspects of the diagnostics applied to the simulation data to determine the nature of radial transport in the presence of radially sheared poloidal flows. In Sec. III, the analysis and interpretation of the numerical ITG data are described. Next, in Sec. IV, we discuss plausible physical mechanisms that could be responsible for the observed transport behaviors. The discussion is mostly speculative in nature at this point. Further simulation efforts are currently underway to test these ideas, which will be published elsewhere in the near future. Finally, some conclusions are drawn in Sec. V.

II. SIMULATIONS

A. The UCAN code

In the simulations that we will examine later, turbulence is driven by the electrostatic ITG mode in toroidal geometry. They have been run using the global particle-in-cell (PIC) gyrokinetic UCAN code. Although UCAN has been described in detail elsewhere[15–17] and has been thoroughly benchmarked with other codes as part of the CYCLONE exercise,[14] some details about the code follow for the sake of completeness. UCAN is a PIC code written in Cartesian coordinates which uses the low noise δf method[18–20] to solve the collisionless, low-β, gyroaveraged kinetic equation in toroidal geometry. As such, it assumes that the distribution function can be expressed as $f=f_0+\delta f$, where f_0 is a Maxwellian containing the background ion density and ion temperature profiles

$$f_0(r,v_\parallel)=n_0\left(2\pi\frac{T_0^i}{m_i}\right)^{-3/2}\exp\left\{-\frac{(m_i/2)v_\parallel^2+\mu B}{T_0^i}\right\}. \tag{1}$$

δf is the non-Maxwellian part. To compute δf, UCAN advances marker ions in time along the nonlinear characteristics in phase space of the ion gyrokinetic equations[18]

$$\dot{\mathbf{R}}=v_\parallel\hat{\mathbf{b}}-\frac{1}{B^2}\left(\frac{\partial\bar{\phi}}{\partial\mathbf{R}}\times\mathbf{B}\right)+\frac{1}{\Omega_i}\left(\mu\nabla B+v_\parallel^2\frac{\hat{\mathbf{b}}\cdot\nabla B}{B}\right), \tag{2}$$

$$\dot{v}_\parallel=-\left[\hat{\mathbf{b}}+\frac{v_\parallel}{\Omega_i}\hat{\mathbf{b}}\times(\hat{\mathbf{b}}\cdot\nabla\hat{\mathbf{b}})\right]\cdot\left(\frac{Ze}{m_i}\frac{\partial\bar{\phi}}{\partial\mathbf{R}}+\mu\cdot\nabla B\right), \tag{3}$$

which include the $\mathbf{E}\times\mathbf{B}$, curvature and ∇B drifts, as well as the mirroring force in the $v_\parallel$ equation. The coupling of the first term on the right-hand side (rhs) of the $v_\parallel$-equation with the third term on the rhs of the $\mathbf{R}$-equation is the so-called parallel nonlinearity, recognized in recent years as an important player in the saturation dynamics.[21] In the δf method each ion also carries a weight $\omega_i\equiv\delta f/f_0$, which is evolved along the characteristic according to

$$\frac{dw_i}{dt}=-(1-w_i)\left[\frac{v_\parallel}{v_{\rm th}}\frac{Ze}{m_i}\frac{\partial\bar{\phi}}{\partial\mathbf{R}}-\frac{1}{B^2}\left(\frac{\partial\bar{\phi}}{\partial\mathbf{R}}\times\mathbf{B}\right)\cdot\left\{\left[\frac{d\ln n_0}{dr}+\frac{(P-3)}{2}\frac{d\ln T_0^i}{dr}\right]\hat{\mathbf{r}}-P\nabla B\right\}\right]. \tag{4}$$

Here, $\hat{\mathbf{b}}\equiv\mathbf{B}/B$, with $\mathbf{B}$ as the magnetic field; $P(v_\parallel,v_\perp)\equiv(2v_\parallel^2+v_\perp^2)/2v_{\rm th}^2$; $v_{\rm th}^2\equiv T_i/m_i$ is the ion thermal velocity; $\Omega_i=ZeB/m_i$ is the ion cyclotron frequency, $\mu=v_\perp^2/2B$ is the magnetic moment, and $\mathbf{R}\equiv\mathbf{r}-\rho$, with the gyroradius defined as $\rho\equiv\mathbf{v}_\perp\times\hat{\mathbf{b}}/\Omega_i$. Finally, $\bar{\phi}(\mathbf{R})\equiv\langle\int d\mathbf{r}\phi(\mathbf{r})\delta(\mathbf{r}-\mathbf{R}-\rho)\rangle_{\rm gp}$ is the gyrophase-averaged electrostatic potential, which is computed numerically via four-point ring averaging.[20]

The self-consistent determination of the plasma evolution requires the electrostatic potential to be obtained from the macroscopic charge density accumulated from the charged particles. UCAN solves the Poisson relation for the low-frequency gyrokinetic system

$$\frac{T_e}{T_i}\frac{(\bar{\phi}-\tilde{\phi})}{\lambda_D^2}=e(Z\bar{n}_i-n_e). \tag{5}$$

Here, the Debye length is $\lambda_D^2=T_e/n_0e^2$; $\tilde{\phi}(\mathbf{r})\equiv\langle\int d\mathbf{R}d\mu dv_\parallel f_0\bar{\phi}(\mathbf{R})\delta(\mathbf{R}-\mathbf{r}+\rho)\rangle_{\rm gp}$. The ion density is obtained from the full numerical distribution function: $\bar{n}(\mathbf{r})\equiv\langle\int d\mathbf{R}d\mu dv_\parallel(f_0+\delta f)\delta(\mathbf{R}-\mathbf{r}+\rho)\rangle_{\rm gp}$. Finally, both passing and trapped electrons are taken to be adiabatic and the electrostatic approximation $n_e=-e(n_0/T_e)(\phi-\bar{\phi}_{00})$ is assumed to hold. $\bar{\phi}_{00}$ represents the surface-averaged fluctuating potential (i.e., it includes both the mean and fluctuating zonal flows). Since electrons are assumed to be adiabatic, UCAN is suitable for studying the heat transported by ITG turbulence but not for quantifying particle transport. In spite of that, we can still use it to characterize the nature of ion transport, as will be shown in what follows. UCAN covers the whole plasma cross section, which is taken to be circular, and is therefore a global code. The implementation in Cartesian coordinates allows the use of fast Fourier transform techniques to solve the gyrokinetic Poisson equation. It has been implemented on massively parallel platforms using domain decomposition along the toroidal direction.[22] The implementation of further domain decomposition within each toroidal slice is currently being developed. Externally driven flows can be included by prescribing an additional external radial electric field $\mathbf{E}_{\rm ext}(r)=-(d\phi^{\rm ext}/dr)\hat{\mathbf{r}}$.

The boundary conditions applied in UCAN are largely historical and set early on in the development of the type of Cartesian global gyrokinetic PIC code that UCAN comes from, both in cylindrical[23] and in toroidal geometries.[24] In each toroidal plane, the particle boundary is a circle whose radius is very close but smaller than the minor radius. The particles meandering outside that circle have their weight set to zero and no longer contribute to the simulation. Because of this buffer zone, it was found convenient through empirical trials early on to adopt periodic boundary conditions for the fields in the X and Y directions. The full set of Fourier modes is kept in the calculations. However, there is a form factor $F(k)=\exp[-(k*a)^6]$, which is applied to the density

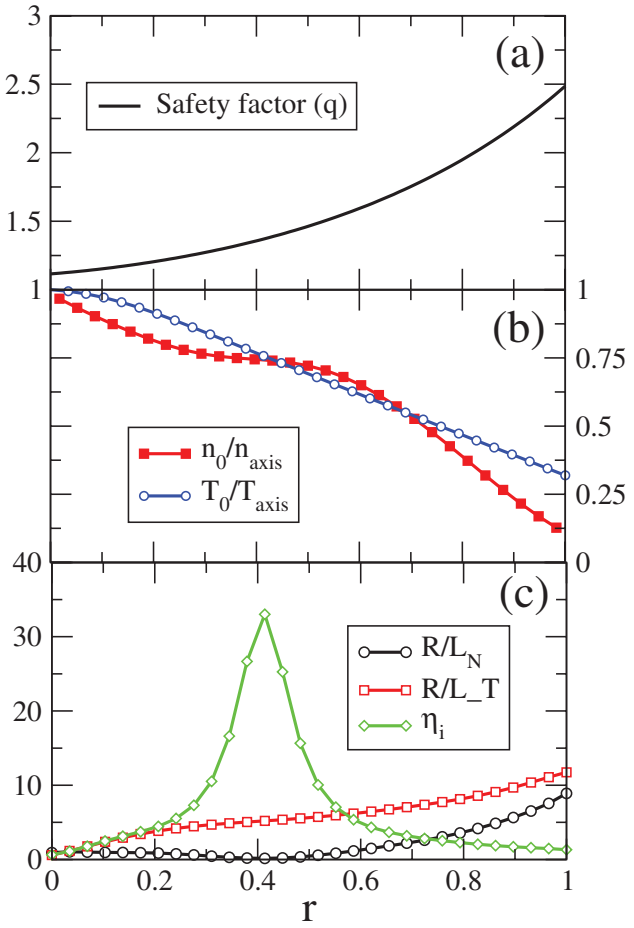

FIG. 1. (Color online) Above: safety factor profile. Middle: density and temperature radial profiles. Bottom: η_i, R/L_T, and R/L_n radial profiles.

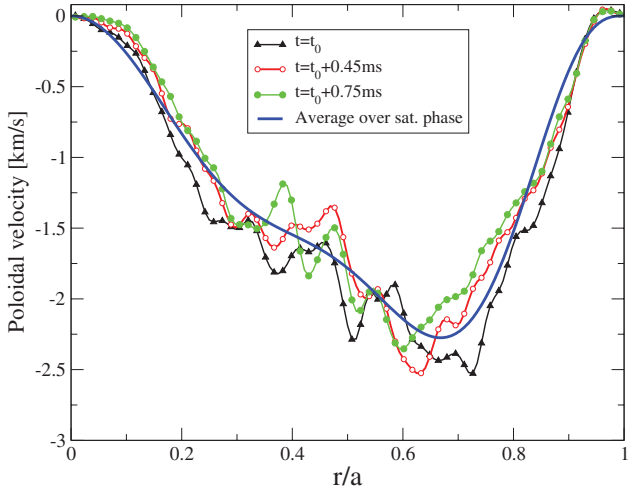

FIG. 2. (Color online) Poloidal velocity profile (solid line) used for simulations with EXT driven flow. For comparison, the instantaneous radial profile of the poloidal velocity obtained in the self-consistent runs is also shown at selected times (see text for a definition of t_0).

when the potential is calculated through the gyrokinetic Poisson equation. Again, this form factor (and the value of a, the particle size, which is of the order of the unit grid spacing) was chosen through empirical trials during the original development of UCAN when it was found to be much less distorting than the more conventional $F(k)=\exp[-(k*a)^2]$ used in standard PIC codes where Gaussian-shaped particles are the norm.

B. ITG simulations used in these studies

The simulations we have used for these studies correspond to collisionless, electrostatic ITG turbulence. The geometry used is a torus with major radius $R=1.7$ m and minor radius $a=0.4$ m. Each location in the torus is labeled by the triad of numbers (r,θ,ζ), r being the radius normalized to a, and θ and ζ the poloidal and toroidal angles (see inset in Fig. 3). The magnetic field used has an axis value $B_0=1.87$ T and the safety factor profile used is shown in Fig. 1(a). Circular magnetic surfaces are assumed. The background density and ion temperature radial profiles used are shown in Fig. 1(b). Axis values for density and temperature $(T_e/T_i=1)$ are, respectively, 3.1×10^{19} m^{-3} and 0.7 keV. The profiles do not go to zero at $r\simeq1$ because these parameters originate from a (higher temperature) simulation carried out previously by some of us to compare against the central 60% of DIII-D tokamak discharges.[25] The profiles chosen are such that the most unstable location is $\sim r\simeq0.4$, where the values of some parameters relevant for ITG turbulence are $R/L_T=5.25$, $R/L_n=0.16$, $q=1.36$, and $\hat{s}\equiv(r/q)(dq/dr)=0.28$. Radial profiles of R/L_T, R/L_n, and $\eta_i(r)\equiv L_n/L_T$ are shown in Fig. 1(c). Computations are done on a Cartesian grid of size $[XYZ]=256\times256\times64$, periodic in Z and including toroidal effects. The radial size of the integration box is $a/\rho_i\sim200$. Time resolution is $dt=0.15$ μs. The Eulerian turbulence decorrelation time [estimated as the $(1/\sqrt{2})$-fold decay time of the autocorrelation of the local fluctuating potential] is typically ~10 μs within the nonlinearly saturated phase. The number of markers used is $\sim3.4\times10^7$ on a spatial grid with $\sim4.2\times10^6$ points, which amounts to eight particles per cell. Although certainly not state of the art, this particle resolution is sufficient to obtain good convergence for our parameters.

Three different sets of simulations have been done for these studies using the parameters just described but differing in their implementation of the zonal flow.[13] The first set has been run in the standard manner: the ITG mode nonlinearly drives the poloidal and toroidal flows that act back on the turbulence until both saturate at some finite levels.[8] In Fig. 3, the electrostatic energy for this case $(E=\int d\mathbf{r}|\bar{\phi}(\mathbf{r})|^2)$ is shown in red. The second simulation that we will discuss has been run by *artificially suppressing* the back reaction of the nonlinearly driven zonal flow by *zeroing* the surface average of the electrostatic potential [i.e., $\phi_{00}(r,t)$] at every time step. As a result, turbulence saturates nonlinearly at a higher energy level (in black, Fig. 3), which results in a larger level of fluctuations and thus in larger radial transport.[15] Finally, in the third type of simulation that we will examine, the zonal flow $\phi_{00}(r,t)$ is still zeroed out, but an external radial electric field is added, such that its related potential $\phi^{\rm ext}(r)$ is roughly equal to the time average over the saturated nonlinear phase of the zonal flow [i.e., $\phi^{\rm ext}(r)$

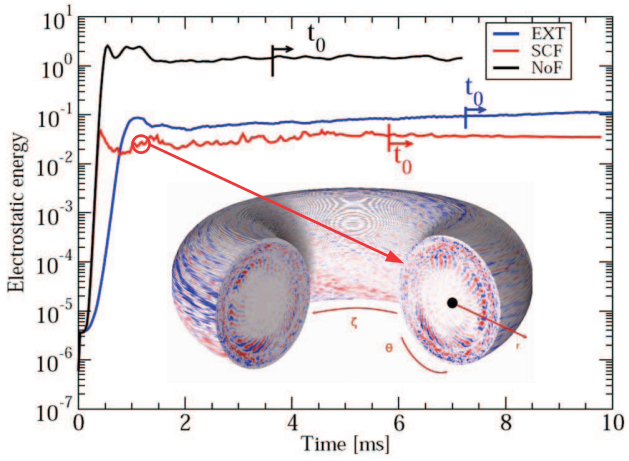

FIG. 3. (Color online) Electrostatic energies for NoF, SCF, and EXT driven flow. Initial t_0 (see text) marked with arrow. Inset: snapshot of temperature fluctuations beyond the linear phase of the self-consistent case just after the zonal flow has already been nonlinearly driven.

$\simeq\langle\phi_{00}(r,t)\rangle_{\rm nl}$] obtained in the first implementation. The radial profile of the resulting externally driven poloidal flow is shown in Fig. 2, together with the instantaneous radial profiles of the poloidal component of zonal flow obtained in the self-consistent case at several times within the saturated phase (the definition of t_0 will be given in Sec. IV). The electric field is ramped up from zero at the start of the simulation, reaching its final value before the nonlinearly saturated phase is reached. Due to the impact of the flow on the

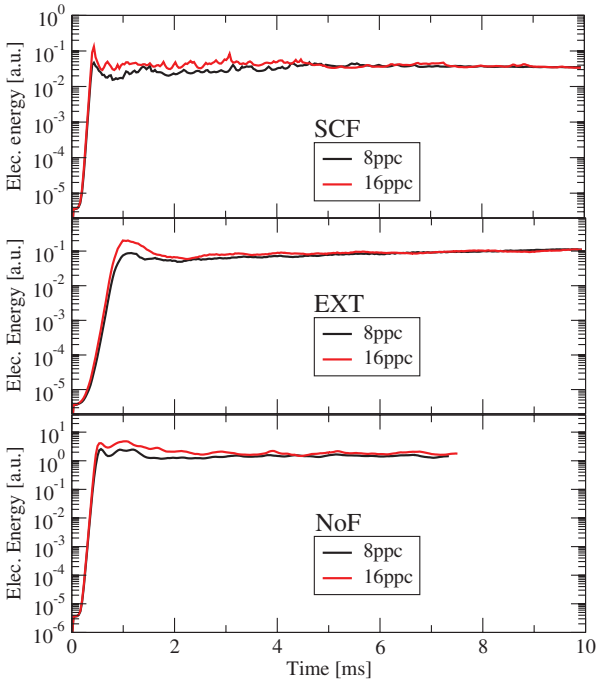

FIG. 4. (Color online) Convergence of UCAN simulations with respect to the number of particles per cell (ppc). All runs have been done with an $[XYZ]=256\times256\times64$ grid. The traces of the total fluctuating electrostatic energy integrated over the whole volume are shown as a function of time. Above: for the SCF case. Middle: for the EXT driven flow case. Below: for the artificially suppressed flow (NoF) case.

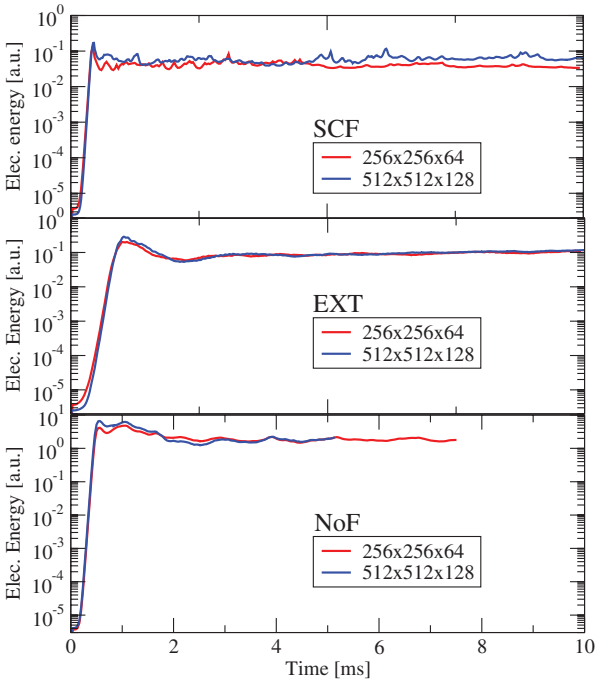

FIG. 5. (Color online) Convergence of UCAN simulations with respect to the grid resolution. All cases have been done using 16 ppc. The traces of the total fluctuating electrostatic energy integrated over the whole volume are shown as a function of time. Above: for the SCF case. Middle: for the EXT driven flow case. Below: for the NoF case.

linear stability properties of the mode, the linear growth phase of this simulation will differ from the other two. However, as the final externally driven flow has roughly the same average strength and radial profile as the self-consistent zonal flow during the nonlinear phase, the electrostatic energy (in blue) saturates at a similar value, as shown in Fig. 3.

In order to test the convergence of the simulations with respect to the number of particles per cell and the grid resolution, we have completed two sets of additional runs for the previous implementations using the same physical parameters. The same grid resolution is kept in the first set (i.e., $[XYZ]=256\times256\times64$), but we use instead 16 particles per cell. Figure 4 shows the time traces of the total electrostatic energy for the self-consistent, externally driven, and artificially suppressed flow cases. The second set of runs probes the convergence with respect to the grid resolution. The number of particles per cell is now kept at 16, and we have then carried out runs with twice the original grid resolution in each toroidal plane and twice the resolution in the parallel direction (i.e., $[XYZ]=512\times512\times128$). Figure 5 shows the time traces of the total electrostatic energy of these simulations for the self-consistent, externally driven, and artificially suppressed flow cases. From these figures, it is concluded that the original run (i.e., $[XYZ]=256\times256\times64$ using eight particles per cell) seems to be fairly well converged.

III. DIAGNOSTICS

The reason UCAN (or any other PIC code for that matter) is particularly useful for our purposes is because the spatial part of the characteristics of the gyrokinetic equation [i.e.,

Eq. (2)] along which the marker ions are being pushed corresponds to the trajectory in real space of the kinetic ion guiding centers. Thus, a large number of realizations of actual ion guiding-center orbits are at our disposal, and they can be used to compute the probability $P_i(r,t|r_0,t_0)$ of finding one ion guiding center at some radius r and time t if it was at another radius r_0 at a previous time $t_0 \leq t$. $P_i(r,t|r_0,t_0)$ is what is known as a *propagator* or, in our case, the *ion guiding-center radial* propagator. As we will show, this propagator can be used to probe the nature of radial transport across sheared zonal flows, despite the fact that UCAN cannot quantify particle transport. Most interestingly, we can investigate the nature of the transport of real ion guiding centers in contrast to what happens when applying a similar methodology to continuum codes (either fluid or gyrokinetic), in which one has to add massless tracers, which are then advected by the turbulent $\mathbf{E}\times\mathbf{B}$ drift.[26–29] UCAN simulated ions also feel all the inertial effects via the (mass and charge dependent) toroidal drifts.

In order to understand how these propagators can be used as a diagnostic, we review first some results from the theory of stochastic transport processes, focusing the discussion on the typical propagator forms which can be expected in different situations. We start with standard diffusion, which is the macroscopic consequence of microscopic Brownian motion. This relationship can be shown, for instance, by constructing a random walk in which particles execute jumps of prescribed length l after having rested at their locations for a prescribed time τ. These typical scales characterize the transport and, in fact, justify its being characterized via a diffusivity $D=l^2/2\tau$. Indeed, the probability of finding one particle at x at time t if initially at x_0 can be found analytically[30] to be ($G[x]$ is a zero mean, unit variance Gaussian law)

$$P_{\mathrm{Bm}}(x,t|x_0,0) = G[(x-x_0)/\sqrt{Dt}]. \tag{6}$$

Thus, the propagator is a Gaussian centered at x_0 with variance which grows as t. The connection with diffusion becomes clear when noting that Eq. (6) is also the solution of $\partial_t n = D\partial_x^2 n$ that satisfies $n(x,0)=\delta(x-x_0)$.

An alternative way of deriving this connection is by starting from the Langevin equation for the position of the particle as a function of time

$$x(t) = x_0 + \int_0^t \xi_2(t')dt'. \tag{7}$$

Here, it is assumed that $\xi_2(t)$ is Gaussian uncorrelated noise, which means that its probability density function (pdf) is Gaussian and its correlation function is $\langle \xi_2(t)\xi_2(t')\rangle = 2D\delta(t-t')$. The particle propagator of Eq. (7), which can be also computed analytically either by computing its moments[31] or by using path-integral methods,[32] is the same as Eq. (6). It is important to note that hidden within the assumption for the correlation function form, typical transport scales have already been introduced. Indeed, noting that the noise is an idealized fluctuating velocity, the correlation function in a real fluid always has a finite width. However, a δ-function is a good representation when the real correlation function decays exponentially with a typical decay time τ. Then, one can use the previous δ-form with $2D \sim V_c^2\tau$, where V_c is a characteristic velocity of the flow. Again, a characteristic length appears, $l \sim \tau/V_c$.

In order to be useful to characterize transport beyond standard diffusion, both the Langevin and the random walk approaches must be generalized. Of particular interest are situations in which typical transport scales are absent but transport still exhibits a self-similar character. (This is a preferred situation, thanks to the same central limit theorem that is behind the widespread application of diffusive transport.) In practical terms, this means that the mean size of transport events in a system of size L diverges as $l \sim L^a$, $a>0$; or that the typical transport time diverges as $\tau \sim T^b$, $b>0$, T being the mean confinement time of particles in it (or the mean life of the system if shorter). This lack of typical scales translates into power-law decaying correlations in both time and space. In cases like these, the generalizations of the random walk and Langevin frameworks just described depart from each other. The random walk is generalized by what is known as the continuous-time random walk (CTRW) introduced by Montroll and Weiss[30] in the 60's and described in detail in the literature.[33–36] Since the appropriate generalization in our case will turn out to stem from the Langevin framework, we do not discuss the details of CTRWs here.

The generalization of the Langevin equation we use is

$$x(t) = x_0 + \frac{1}{\Gamma\left(H-\frac{1}{\alpha}+1\right)}\int_0^t dt'(t-t')^{H-1/\alpha}\xi_\alpha(t'), \tag{8}$$

with $H \in (0,1]$ and $\alpha \in (0,2]$, and $\Gamma(x)$ being Euler's gamma function. H is known as the *self-similarity exponent* (or *transport exponent*). Let us start with the case $\alpha=2$. Then, Eq. (8) reduces to the fractional Brownian motion (fBm) introduced by Mandelbrot and van Ness[31] in the late 60's, which reduces to the usual Brownian motion [Eq. (7)] when $H=1/2$. (It must be noted that Mandelbrot gives preference to an alternate formulation of fBMs, which does not give so much importance to the initial time $t=0$ and which might thus be argued to be more adequate. But since both formulations yield the same propagators, the precise choice is unimportant for the discussion that follows.) But in contrast to Brownian motion, the successive increments $dx(t) := x(t+dt)-x(t)$ of fBm are correlated in time in such a way that no finite typical time scale exists if $H \neq 1/2$. That is, there is no time scale beyond which the motion becomes insensitive to its previous history. The fBm propagator can be found analytically to be[31,32]

$$P_{\mathrm{fBm}}(x,t|x_0,0) = G\left[(2H)^{1/2}\Gamma\left(H+\frac{1}{2}\right)\frac{(x-x_0)}{D^{1/2}t^H}\right]. \tag{9}$$

The propagator is still a Gaussian, but now note that the variance $\sigma^2 \sim t^{2H}$. By comparison with the usual (diffusive) Brownian motion, it follows that the motion is subdiffusive for $H<1/2$ and superdiffusive for $H>1/2$. In the first case, successive velocities have become anticorrelated in the sense that the probability of the next velocity value having an opposite sign is larger than that of retaining the same sign. In

contrast, for $H>1/2$, the probability is larger for staying on course, so that the successive velocities are positively correlated. The existence of this "memory" is what causes the loss of the characteristic time scale τ, which is no longer well defined.

However, fBm still has a well-defined characteristic velocity V_c^2, resulting from the finite variance of the noise pdf. This is no longer the case when $\alpha<2$, which means that the statistics of the uncorrelated noise ξ_α follow a symmetric Lévy form.[37] This choice of statistics converts Eq. (8) in what is known as fractional Lévy motion (fLm). It is a very natural choice because Lévy laws are stable distributions that happen to satisfy the same central limit theorem as the Gaussian law. Thus, they should also be expected to become a preferred distribution in nature. But Lévy laws decay instead algebraically for large values of their arguments as power laws with exponent $-(1+\alpha)$, $\alpha\in(0,2)$. Because of this algebraic decay, they have an infinite variance so that the characteristic velocity V_c, which still existed for fBm, can no longer be defined. The fLm propagator can also be computed analytically,[38,39] the result being ($L_\alpha[x]$ is a symmetric Lévy law of index α and scale factor unity)

$$P_{\mathrm{fLm}}(x,t|x_0,0)=L_\alpha\left[(\alpha H)^{1/\alpha}\Gamma\left(\frac{\alpha H-1+\alpha}{\alpha}\right)\frac{(x-x_0)}{D^{1/\alpha}t^H}\right]. \tag{10}$$

Note that Eq. (10) reduces to the fBm result if $\alpha=2$ and to Brownian motion if, in addition, $H=1/2$. Although we will still use the subdiffusive or superdiffusive terminology in the same way as with fBm (that is, depending on whether H is smaller or larger than 1/2), note that the successive displacements of motion are now uncorrelated only when $H=1/\alpha$, anticorrelated if $H<1/\alpha$, and positive correlated otherwise. Note also that the only finite moments of fLm have order $s<\alpha$ and grow as t^{sH}. But the variance can still be computed in a finite system of size L. It would scale as in the fBm case $\sigma^2\sim Ct^{2H}$, but C would diverge now with the system size.

The way we will diagnose the nature of transport will be by comparing the numerically obtained radial propagators for the ion guiding centers with the analytic forms just discussed. These forms all have a well-defined physical meaning. A practical warning, which may seem unnecessary but which is often ignored in the literature, is made at this point regarding how this comparison must be carried out. Propagators should not be compared by plotting the numerical and analytical forms in the same linear-linear plot because the central part of a Lévy law looks very much like a Gaussian in lin-lin scale, specially if the Lévy index is not far from 2, the Gaussian value (see Fig. 6). Thus, it is extremely important to carry out such comparison using a log-linear plot and to use a fitting procedure based on the minimization of some figure of merit. In our case, we use a Levenberg–Marquard algorithm to minimize a target (chi-square) function built as the sum (over all binned values) of the squared difference between the numerical and analytical propagators normalized to the analytical value.

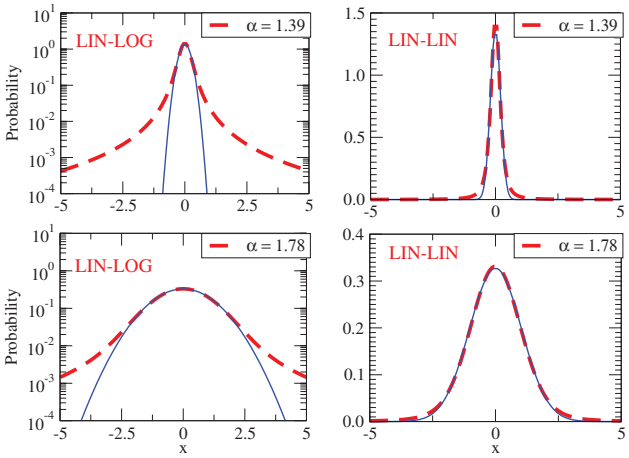

FIG. 6. (Color online) Comparison between two Lévy laws ($\alpha=1.39$ above; $\alpha=1.78$ below) and the Gaussian fits to their central parts. Left: linear-log scale. Right: linear-linear scale. Note that to tell them apart "experimentally" one needs to resolve probabilities as low as 10^{-1} for $\alpha=1.39$ and 10^{-2} for $\alpha=1.78$. As $\alpha\to2^-$, the probability that needs to be resolved tends rapidly to zero.

IV. RESULTS

With the analytical propagators just discussed in Sec. III in mind, we now discuss the ion guiding-center radial propagators obtained for the three simulations described in Sec. II. For the analysis to be meaningful, the ion guiding-center motion is considered only for times well within the nonlinearly saturated phase. This is important as results from the nonstationary parts of the simulation may be misinterpreted as features that are characteristic of the steady-state transport dynamics. The starting time (t_0) used for each case is marked with horizontal arrows in Fig. 3. Furthermore, we restrict the analysis to those ions present at t_0 within a narrow annulus (i.e., $r\in[0.35-0.40]$) close to where the instability drive is maximum, and to elapsed times, $\Delta t\equiv t-t_0$, not too long (compared with the simulation duration) but still larger than a meaningful number of eddy turnover times. In this way, two difficulties that can make the results complicated to interpret can be avoided. First, by not considering the shortest times we avoid distortions of the propagator for values of the radial displacement ($\Delta r\equiv r-r_0$) up to the average banana width and elapsed times up to the mean inverse bouncing frequency (~0.2 ms) caused by the fact that a fraction of the ions will follow the trapped orbits.[40] Second, we avoid having to deal with the effect of spatial inhomogeneities in the turbulence which would become apparent at long times if particles had time to move into regions in which the turbulence is very different.

Snapshots of the numerical propagators are shown in Fig. 7 for three different Δt values (with respect to the initial time t_0) chosen to be large enough to exceed the trapped-ion distorted regime for the three simulations described in Sec. II. Figure 7(a) shows the snapshots of the propagator for the case with artificially suppressed zonal flow, which clearly follows a Gaussian form (as shown by the fits included in the figure in dashed lines) that spreads with time. Figure 7(b) shows the snapshots of the propagator for the case in which

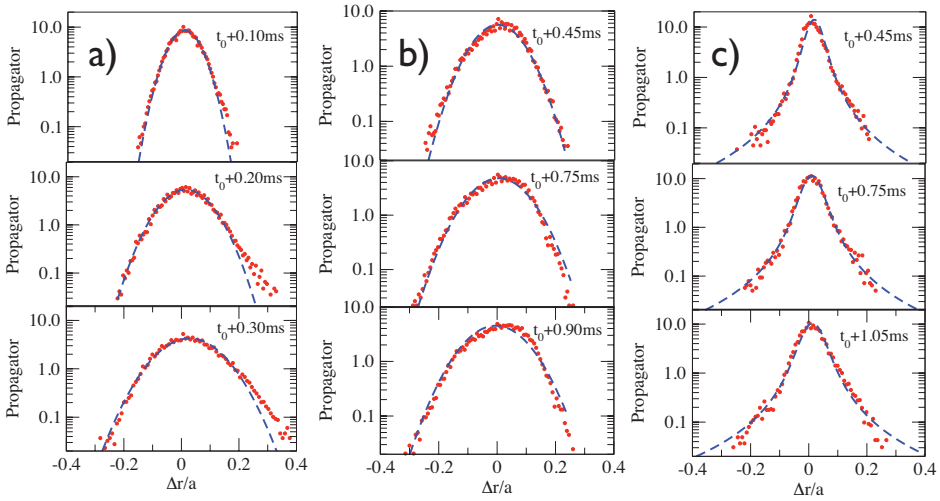

FIG. 7. (Color online) Snapshots of the ion guiding-center radial propagators at three different times for NoF (left), EXT driven flow (center), and SCF (right). Best fits shown in dashed lines: Lévy fit on the right frame corresponds to $\alpha=1.42$; other fits are Gaussian.

the zonal flow driven by turbulence has also been artificially suppressed, and it is substituted by an externally driven flow of similar strength and profile. The result is again a set of Gaussian propagators, but note that the spreading of the propagator seems to take place at a much slower pace. (We will see in what follows that this slower pace cannot be interpreted as a reduced diffusivity relative to the case with all flows suppressed.) Finally, Fig. 7(c) shows the snapshots of the propagator for the usual UCAN setup: the case in which a zonal flow is driven nonlinearly by the turbulence, which acts back on the fluctuations until a saturated state is reached. The result is somewhat surprising: it is clearly non-Gaussian and its convexity reverses so that it exhibits an algebraic tail that decays as $\sim(\Delta r)^{-2.4}$. By carrying out a simple Lévy fit for a sequence of successive Δt, one concludes that the propagator is fitted extremely well by a symmetric Lévy law with $\alpha=1.42$.

Next, we discuss the time scaling of the variances (i.e., $\sigma^2\equiv\langle(\Delta r)^2-\langle\Delta r\rangle^2\rangle$) of the propagators for the three cases, since the form of the propagator is not sufficient to characterize the nature of transport. The variances are plotted as a function of Δt in Fig. 8. The effect of the trapped ions is apparent for cases with zonal flows up to $\Delta t\sim 0.1-0.3$ ms. The distortion, however, is absent in the case with no zonal flow because the larger (unsuppressed) fluctuations kick ions out of their trapped orbits before they complete the banana. For the run in which the zonal flow has been artificially suppressed, the variance (black, Fig. 8) scales as $\sigma^2\sim t$. But for the other two cases, in both of which a zonal flow exists, the variance scales instead sublinearly with time, which is a signature of subdiffusion. Indeed, $\sigma^2\sim t^{0.5}$ for time scales exceeding both the turbulence decorrelation time and the ion bouncing time for the externally driven flow case [blue (or dark gray in the print version), Fig. 8]. Similarly, $\sigma^2\sim t^{0.7}$ for the case with the self-consistent zonal flow [red (or gray in the print version), Fig. 8].

Comparing these numerical propagators with the analytical propagators introduced in Sec. III, we conclude that the results strongly suggest that the nature of radial turbulent transport is diffusive only in the absence of any radially sheared poloidal flow, since the propagator then follows a Gaussian form and its variance increases linearly with time. (That is, using the transport exponents introduced in Sec. III, $\alpha=2$ and $H=1/2$, for this case.) However, the nature of radial transport is very different in the presence of a sheared poloidal flow, either externally driven or nonlinearly driven by the turbulence itself. In the externally driven case, the propagator is still Gaussian (i.e., $\alpha=2$), but it spreads sublinearly with time, being consistent with fBm with $H=0.25\pm0.03$ and not with diffusion within the intermediate time scales and up to the simulation end. Physically, this result means that the ion radial velocities somehow self-correlate over long times so that the probability of reversing their sign exceeds that of retaining it. Finally, the case with the self-consistent zonal flow is even more different. The propagator variance has been found to be subdiffusive (with $H\sim0.34$) in the intermediate range, suggesting that a finite typical time scale is again absent as in the externally driven case. But it is not fBm, since the propagator is clearly not Gaussian, but follows instead a Lévy law. Fat tails are characteristic of situations without a finite typical length scale l.

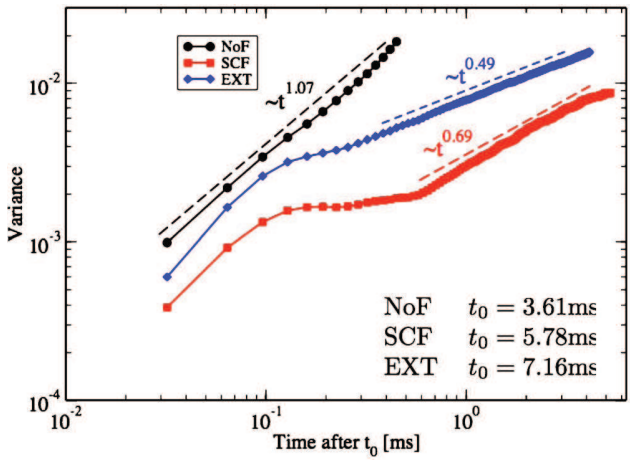

FIG. 8. (Color online) Variance of ion guiding-center radial propagators as a function of the elapsed time after t_0 for cases with NoF, SCF, and EXT driven flow. The values of t_0 used for each case are listed in the lower right corner.

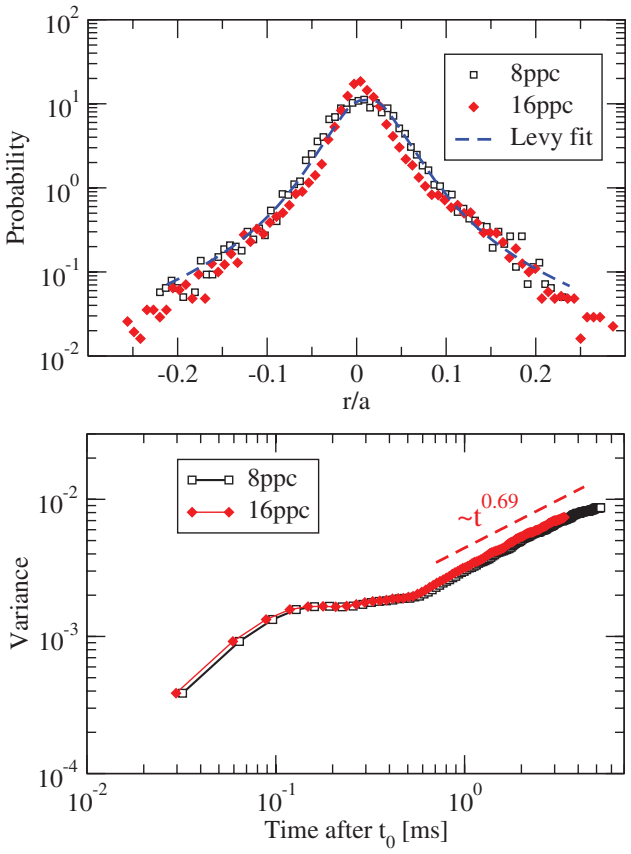

FIG. 9. (Color online) Example of convergence of the transport analysis with respect to the number of ppc for the SCF case. Ion guiding-center radial propagators are shown (above) at t_0+1 ms (a Lévy fit with $\alpha=1.42$ is included for comparison); variance of propagators is also shown as a function of time (below).

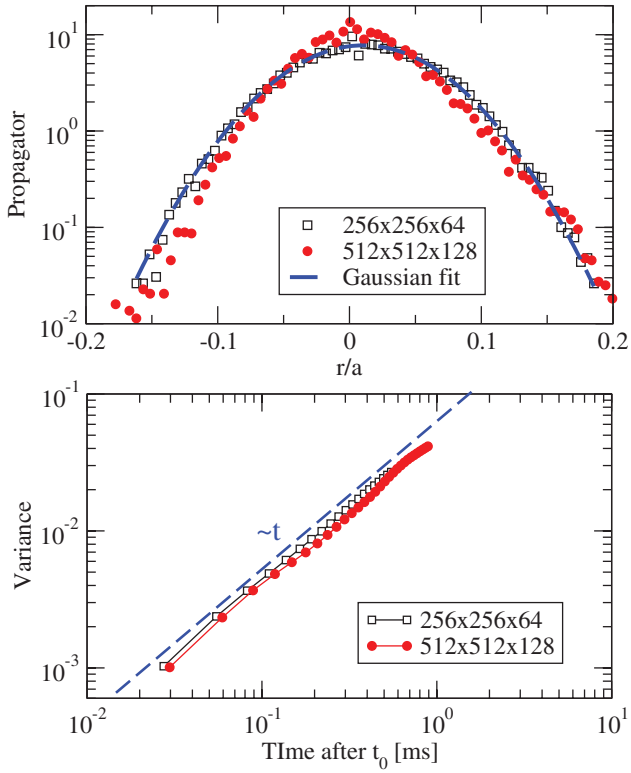

FIG. 10. (Color online) Example of convergence of the transport analysis with respect to grid resolution for the NoF case. Ion guiding-center radial propagators are shown (above) at $t_0+0.12$ ms (a Gaussian fit is included for comparison); variance of propagators is also shown as a function of time (below).

Thus, the radial transport appears to lack both spatial and temporal typical scales and is consistent with fLm with $\alpha=1.42\pm0.04$ and $H=0.34\pm0.03$.

Although the discussion in this section has been made using the propagators and variances obtained from the runs with eight particles per cell and an $[XYZ]=256\times256\times64$ grid, we have repeated the same analysis on the higher resolution runs done to test the level of convergence of our simulations. As an illustration, Fig. 9 compares the propagators and variances obtained for the self-consistent flow case with the same grid resolution ($[XYZ]=256\times256\times64$) but 8 and 16 particles per cell. Similarly, Fig. 10 shows the same comparison but between two runs of the artificially suppressed flow case with 16 particles per cell but two different grid resolutions: $[XYZ]=256\times256\times64$ and $[XYZ]=512\times512\times128$. The values of the exponents α and H obtained during this convergence exercise for these two comparisons as well as all other cases examined have been collected in Table I. The level of convergence is quite satisfactory.

V. DISCUSSION

In this section, we propose and briefly discuss a physical mechanism plausibly responsible for the onset of nondiffusive radial transport reported in this paper. In particular, we will focus on the mechanism causing subdiffusion, which is present in both the externally and self-consistently driven cases. The character of the discussion is speculative since hard numerical evidence from gyrokinetic simulations is still being gathered with UCAN. However, some supporting numerical evidence has been obtained using a simpler drift-

TABLE I. Exponents α and H obtained at the same positions and times for various UCAN simulations with the same parameters but varying particle and/or grid resolution. Electrostatic energies, propagators, and variances for some of these runs are illustrated in Figs. 4, 5, 9, and 10.

Particles per cell	Grid	α	H
Self-consistent flow			
8	$256\times256\times64$	1.42 ± 0.04	0.34 ± 0.03
16	$256\times256\times64$	1.47 ± 0.09	0.36 ± 0.05
16	$512\times512\times128$	1.48 ± 0.07	0.36 ± 0.04
Externally driven flow			
8	$256\times256\times64$	2	0.25 ± 0.03
16	$256\times256\times64$	2	0.26 ± 0.05
16	$512\times512\times128$	2	0.28 ± 0.05
Artificially suppressed flow			
8	$256\times256\times64$	2	0.50 ± 0.03
16	$256\times256\times64$	2	0.51 ± 0.06
16	$512\times512\times128$	2	0.49 ± 0.04

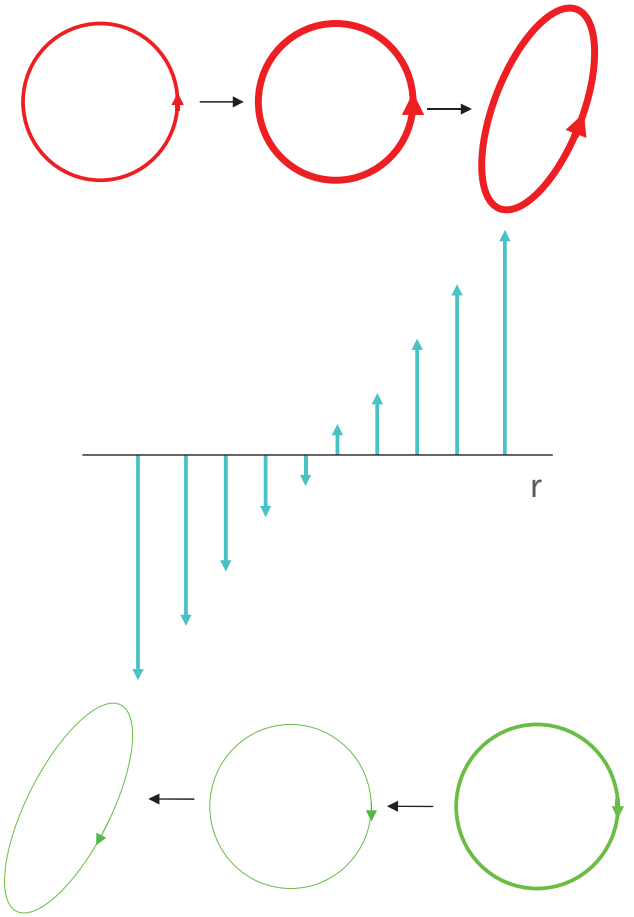

FIG. 11. (Color online) Sketch of the generation of preferential vorticity sign and eddy tilting caused by a sheared flow. Thickness of the line represents the strength of the eddy (i.e., the absolute value of the axial vorticity it contains). The direction of circulation distinguishes between different axial vorticity signs: positive (above) and negative (below).

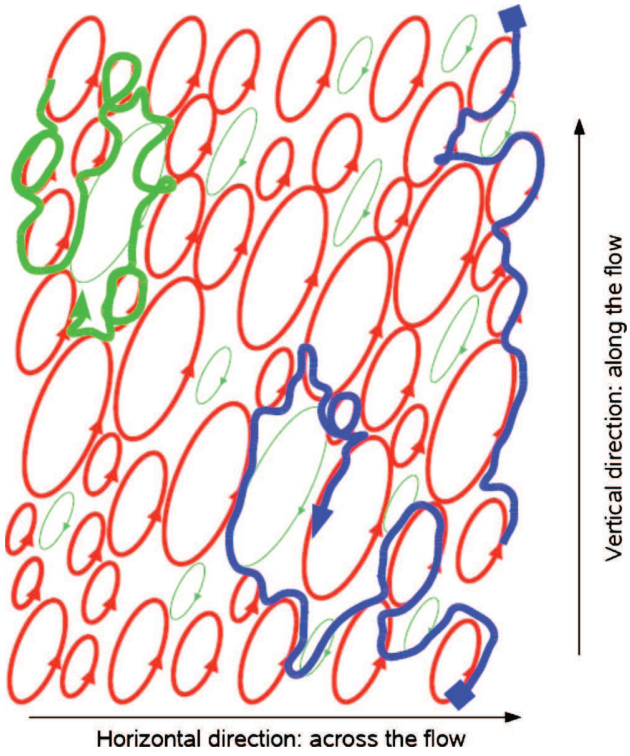

FIG. 12. (Color online) Sketch of motion in the presence of preferential vorticity and eddy tilting. Here, the vertical direction is assumed to be periodic and the periodic continuation of a trajectory is represented by a square. The component of the particle velocity perpendicular to the sheared flow has a larger probability of reversing its direction (over time scales longer than an eddy turnover time) than staying on the same course.

wave turbulence code in slab geometry, which incorporates the action of an externally driven sheared flow.[41] These results give us confidence in the validity of the mechanism we propose to explain the subdiffusion, although its details will need to be revised to accommodate the toroidal geometry of the UCAN simulations.

To understand this mechanism, let us consider how transport across a sheared flow is modified by the action of a shear flow on the underlying two-dimensional turbulence. First, a preferential sign of the axial vorticity appears coming from the sign of the vorticity of the sheared flow; second, the turbulent eddies are tilted with the flow. In Fig. 11, a sketch of an x-sheared y-directed flow is shown from which the mean flow has been subtracted. The effect of a positively sheared flow on those eddies with positive (above) and negative (below) axial vorticities (along z, which comes out of the plane of the figure) is also illustrated. Both types of eddies are going to be tilted in the direction of the flow, thus reducing the mean eddy size along the direction perpendicular to the flow (i.e., along x). Importantly and simultaneously, those eddies with positive axial vorticities will also be reinforced by the positively sheared flow, while those with negative vorticities will be weakened and partially suppressed. Note that these two effects persist even if the eddies are eventually sheared apart. Thus, in the presence of the sheared flow, the motion of any particle advected by the turbulence will take place within a landscape in which a preferential sign for the axial vorticity exists (positive in the case sketched in Fig. 12). A couple of trajectories of particles moving across such a landscape have also been sketched in the figure. Note that whenever the particle leaves the eddy in which it is being advected (say, due to either the eddy being torn away by nearby eddies or to inertial effects), the probability of being advected next by an eddy with the same sign of the axial vorticity (as that of the one just left) is larger than the probability of being advected next by an eddy with axial vorticity of the opposite sign. Note that the difference between the two probabilities will become larger as the shear becomes stronger, since the imbalance between positive and negative vorticities will be also greater. In terms of the particle velocity along the x-direction, this causes that the probability of reversing the sign of its x-velocity over time scales longer than an eddy turnover time is larger than that of staying with the same sign (see Fig. 12). As discussed in Sec. III, the presence of an asymmetry slanted toward changing the direction of motion is the cause of subdiffusion. In contrast, in the absence of the sheared flow, the populations of eddies with either sign of axial vorticity would be roughly equal and the probability of the advected particle changing or not the sign of its x-velocity would thus be the same. Thus, diffusion

would ensue. It is important to stress that the mechanism we propose for subdiffusion would work on all turbulent scales that are affected by the shear. The fact that eddies may be sheared apart by the flow does not invalidate the argument in any way. Also, note that it is the existence of a preferential vorticity sign that makes it work. The tilting of the eddies reinforces the subdiffusive effect by causing an overlap of the eddies, but it would not be sufficient by itself to establish it.

The previous discussion suggests that in the case of the UCAN simulations, subdiffusion in the radial direction is caused mainly by the shear of the time-averaged (over the nonlinearly saturated phase) poloidal zonal flow. Indeed, this conclusion seems to be in agreement with the observation that both the externally driven and the self-consistent UCAN simulations showed radial subdiffusion. Finally, note that the main difference between the self-consistent and externally driven cases is whether the fluctuating (in time) part of the zonal flow is kept or not. This suggests that the mechanism responsible for the appearance of Lévy radial propagators observed in the simulations should probably be related to the shear of the fluctuating (in time) component of the zonal flow. The details of how and why this happens are still under investigation.

VI. CONCLUSIONS

We have reported the first numerical evidence that suggests that the traditional assumption of the diffusive nature of radial transport in magnetically confined toroidal plasmas is challenged in the presence of sheared zonal flows, driven either self-consistently by the turbulence or externally. In particular, our simulations show that radial transport remains subdiffusive for a large range of scales beyond the turbulent decorrelation time. Furthermore, the transport exhibits non-Gaussian features in the self-consistent case. Although the phenomenology is robust, the actual value of the exponents α and H depends on the strength and length scale of the shear of the flow. The weaker the shear, the more diffusive-like transport will behave.

Our findings should have an important practical impact if one is interested in quantifying transport across sheared flows for time scales over which the subdiffusive behavior dominates. How long these time scales do extend would probably be different in each situation, since it should depend on the characteristics of the shear of the flow. In the simulations we have examined, the transition to a different transport regime has not been observed, which implies that the subdiffusive range is at least an order of magnitude longer than the eddy turnover time for those runs. It should however be expected that either diffusive or superdiffusive transport will take over at some point. Otherwise no steady state would be possible, since subdiffusion implies that any continuous external fueling would result in a steady buildup of the profiles. Whether it would be diffusion or superdiffusion may depend on the role played by the background profile evolution that feeds free energy to the instabilities. For instance, in near-marginal turbulence, superdiffusive behavior should probably be expected.[42–45] But even in cases in which diffusive behavior may finally dominate at the longer time scales, the actual diffusivity may be considerably smaller in the presence of sheared flows compared to that which would be naively estimated using quasilinear arguments that assume diffusion at the shorter time scales. (Although one could also envision situations in which some other mechanism ensures a steady state without reaching the long time scales needed to overcome the domination of subdiffusion. For instance, this might happen in H-mode discharges with edge localized modes (ELMs) during the ELM-free periods. The strong poloidal shear present in the pedestal may result in subdiffusive transport, which causes the continuous buildup of profiles between ELMs. Before reaching the times at which diffusion (or superdiffusion) dominates, and when a steady-state profile can be sustained, an instability is triggered that causes the ELM and thus maintains a quasisteady state via quasiperiodic relaxations of the profiles.)

It should also be noted that the Lévy tails observed in the case with the self-consistent flow may have important implications for both control and design for edge flux loads. When calculating the particle and heat loads, it is not just the average load that is important but also the instantaneous load (or the probability distribution of the instantaneous loads). This distribution of loads can be radically changed by the bursty Lévy-type transport events when contrasted to a Gaussian distribution of transport events. These results in turn suggest that externally imposed flows might be useful in controlling the distribution of heat and particle loads, even given the same average flux (load).

Due to the generality of the suppression of transport via sheared flows, our conclusions should be applicable beyond the context discussed here, including astrophysical, atmospheric, and oceanic stable sheared flows. They also might open up interesting avenues in the area of plasma control. Finally, it is worth noting that the fact that fBm/fLm fits so well the radial propagators from our simulations elegantly connects with recent theoretical work showing that under similar assumptions for a prescribed turbulent flow, the transport of any passive quantity becomes nondiffusive and can be analytically obtained in terms of fractional differential equations.[46]

ACKNOWLEDGMENTS

Research was carried out at Oak Ridge National Laboratory, managed by UT-Battelle LLC, for U.S. DOE under Contract No. DE-AC05-00OR22725. Research was funded by the DOE Office of Science Grant No. DE-FG02-04ER54741 at University of Alaska and Grant No. DE-FG02-04ER54740 at UCLA. Simulations run, thanks to grants for use of supercomputing resources at the University of Alaska's Arctic Region Supercomputing Center in Fairbanks, DOE's National Energy Research Scientific Computing Center (NERSC) in Berkeley, and the Spanish National Supercomputing Network (RES) in Barcelona and Madrid.

[1]F. Wagner, G. Becker, K. Behringer, D. Campbell, A. Eberhagen, W. Engelhardt, G. Fussmann, O. Gehre, J. Gernhardt, G.v. Gierke, G. Haas, M. Huang, F. Karger, M. Keilhacker, O. Klüber, M. Kornherr, K. Lackner,

G. Lisitano, G. G. Lister, H. M. Mayer, D. Meisel, E. R. Müller, H. Murmann, H. Niedermeyer, W. Poschenrieder, H. Rapp, H. Röhr, F. Schneider, G. Siller, E. Speth, A. Stäbler, K. H. Steuer, G. Venus, O. Vollmer, and Z. Yü, Phys. Rev. Lett. **49**, 1408 (1982).
[2]K. H. Burrell, Phys. Plasmas **4**, 1499 (1997).
[3]J. W. Connor, T. Fukuda, X. Garbet, C. Gormezano, V. Mukhovatov, M. Wakatani, ITB Database Group, and ITPA Topical Group on Transport and Internal Barrier Physics, Nucl. Fusion **44**, R1 (2004).
[4]H. Biglari and P. H. Diamond, Phys. Fluids B **2**, 1 (1990).
[5]P. W. Terry, Rev. Mod. Phys. **72**, 109 (2000).
[6]P. H. Diamond, S.-I. Itoh, K. Itoh, and T. S. Hahm, Plasma Phys. Controlled Fusion **47**, R35 (2005).
[7]B. A. Carreras, V. E. Lynch, L. Garcia, and P. H. Diamond, Phys. Fluids B **5**, 1491 (1993).
[8]Z. Lin, T. S. Hahm, W. W. Lee, W. M. Tang, and R. B. White, Science **281**, 1835 (1998).
[9]E. J. Doyle, W. A. Houlberg, Y. Kamada, V. Mukhovatov, T. H. Osborne, A. Polevoi, G. Bateman, J. W. Connor, J. G. Cordey, T. Fujita, X. Garbet, T. S. Hahm, L. D. Horton, A. E. Hubbard, F. Imbeaux, F. Jenko, J. E. Kinsey, Y. Kishimoto, J. Li, T. C. Luce, Y. Martin, M. Ossipenko, V. Parail, A. Peeters, T. L. Rhodes, J. E. Rice, C. M. Roach, V. Rozhansky, F. Ryter, G. Saibene, R. Sartori, A. C. C. Sips, J. A. Snipes, M. Sugihara, E. J. Synakowski, H. Takenaga, T. Takizuka, K. Thomsen, M. R. Wade, H. R. Wilson, ITPA Transport Physics Topical Group, ITPA Confinement Database and Modelling Topical Group, and ITPA Pedestal and Edge Topical Group, Nucl. Fusion **47**, S18 (2007).
[10]F. Wagner, J. Baldzuhn, R. Brakel, R. Burhenn, V. Erckmann, T. Estrada, P. Grigull, H. H. Hartfuss, G. Herre, M. Hirsch, J. V. Hofmann, R. Jaenicke, A. Rudyi, U. Stroth, and A. Weller, Plasma Phys. Controlled Fusion **36**, A61 (1994).
[11]V. Antoni, E. Spada, N. Vianello, M. Spolaore, R. Cavazzana, G. Serianni, and E. Martines, Plasma Phys. Controlled Fusion **47**, B13 (2005).
[12]P. W. Terry, D. E. Newman, and A. S. Ware, Phys. Rev. Lett. **87**, 185001 (2001).
[13]R. Sanchez, D. E. Newman, J.-N. Leboeuf, V. K. Decyk, and B. A. Carreras, Phys. Rev. Lett. **101**, 205002 (2008).
[14]A. M. Dimits, B. I. Cohen, N. Mattor, W. M. Nevins, D. E. Shumaker, S. E. Parker, and C. Kim, Nucl. Fusion **40**, 661 (2000).
[15]J. N. Leboeuf, J. M. Dawson, V. K. Decyk, M. W. Kissick, T. L. Rhodes, and R. D. Sydora, Phys. Plasmas **7**, 1795 (2000).
[16]R. D. Sydora, V. K. Decyk, and J. M. Dawson, Plasma Phys. Controlled Fusion **38**, A281 (1996).
[17]J. C. Kniep, J. N. Leboeuf, and V. K. Decyk, Comput. Phys. Commun. **164**, 98 (2004).
[18]T. S. Hahm, Phys. Fluids **31**, 2670 (1988).
[19]A. M. Dimits and W. W. Lee, J. Comput. Phys. **107**, 309 (1993).
[20]W. W. Lee, J. Comput. Phys. **72**, 243 (1987).
[21]L. Villard, S. J. Allfrey, A. Bottino, M. Brunetti, G. L. Falchetto, V. Grandgirard, R. Hatzky, J. Nuhrenberg, A. G. Peeters, O. Sauter, S. Sorge, and J. Vaclavik, Nucl. Fusion **44**, 172 (2004).
[22]V. K. Decyk and C. D. Norton, Comput. Phys. Commun. **164**, 80 (2004).
[23]R. D. Sydora, T. S. Hahm, W. W. Lee, and J. M. Dawson, Phys. Rev. Lett. **64**, 2015 (1990).
[24]S. E. Parker, W. W. Lee, and R. A. Santoro, Phys. Rev. Lett. **71**, 2042 (1993).
[25]C. L. Rettig, T. L. Rhodes, J. N. Leboeuf, W. A. Peebles, E. J. Doyle, G. M. Staebler, K. H. Burrell, and R. A. Moyer, Phys. Plasmas **8**, 2232 (2001).
[26]B. A. Carreras, V. E. Lynch, and G. M. Zaslavsky, Phys. Plasmas **8**, 5096 (2001).
[27]D. del-Castillo-Negrete, B. A. Carreras, and V. E. Lynch, Phys. Rev. Lett. **94**, 065003 (2005).
[28]T. Hauff and F. Jenko, Phys. Plasmas **13**, 102309 (2006).
[29]J. A. Mier, R. Sanchez, L. Garcia, B. A. Carreras, and D. E. Newman, Phys. Rev. Lett. **101**, 165001 (2008).
[30]E. W. Montroll and G. Weiss, J. Math. Phys. **6**, 167 (1965).
[31]B. Mandelbrot and J. van Ness, SIAM Rev. **10**, 422 (1968).
[32]I. Calvo and R. Sanchez, J. Phys. A: Math. Theor. **41**, 282002 (2008).
[33]R. Metzler and J. Klafter, Phys. Rep. **339**, 1 (2000).
[34]G. M. Zaslavsky, Phys. Rep. **371**, 461 (2002).
[35]B. Ph. van Milligen, R. Sanchez, and B. A. Carreras, Phys. Plasmas **11**, 2272 (2004).
[36]R. Sanchez, B. Ph. van Milligen, and B. A. Carreras, Phys. Plasmas **12**, 056105 (2005).
[37]G. Samorodnitsky and M. S. Taqqu, *Stable Non-Gaussian Processes* (Chapman and Hall, London, 1994).
[38]N. Laskin, I. Lambadaris, F. C. Harmantzis, and M. Devetsikiotis, Comput. Netw. **40**, 363 (2002).
[39]I. Calvo, R. Sanchez, and B. A. Carreras, J. Phys. A: Math. Theor. **42**, 055003 (2009).
[40]F. L. Hinton and R. D. Hazeltine, Rev. Mod. Phys. **48**, 239 (1976).
[41]D. E. Newman, D. Samaddar, R. Sanchez, and B. A. Carreras, in *Proceedings of the 35th European Physical Society Conference on Plasma Physics*, Hersonissos, 9–13 June 2008, Vol. 32, p. 1.044.
[42]P. H. Diamond and T. S. Hahm, Phys. Plasmas **2**, 3640 (1995).
[43]D. E. Newman, B. A. Carreras, P. H. Diamond, and T. S. Hahm, Phys. Plasmas **3**, 1858 (1996).
[44]R. Sanchez, D. E. Newman, and B. A. Carreras, Nucl. Fusion **41**, 247 (2001).
[45]B. A. Carreras, D. E. Newman, V. E. Lynch, and P. H. Diamond, Phys. Plasmas **3**, 2903 (1996).
[46]R. Sanchez, B. A. Carreras, D. E. Newman, V. E. Lynch, and B. Ph. van Milligen, Phys. Rev. E **74**, 016305 (2006).